



# Rational design on 3D hierarchical bismuth oxyiodides via *in situ* self-template phase transformation and phase-junction construction for optimizing photocatalysis against diverse contaminants

Hongwei Huang <sup>a,\*</sup>, Ke Xiao <sup>a</sup>, Tierui Zhang <sup>b</sup>, Fan Dong <sup>c</sup>, Yihe Zhang <sup>a,\*</sup>

<sup>a</sup> Beijing Key Laboratory of Materials Utilization of Nonmetallic Minerals and Solid Wastes, National Laboratory of Mineral Materials, School of Materials Science and Technology, China University of Geosciences, Beijing, 100083, China

<sup>b</sup> Key Laboratory of Photochemical Conversion and Optoelectronic Materials, Technical Institute of Physics and Chemistry, Chinese Academy of Sciences, Beijing, 100190, China

<sup>c</sup> Chongqing Key Laboratory of Catalysis and Functional Organic Molecules, College of Environmental and Bio-logical Engineering, Chongqing Technology and Business University, Chongqing, 400067, China



## ARTICLE INFO

### Article history:

Received 30 July 2016

Received in revised form 6 October 2016

Accepted 29 October 2016

Available online 31 October 2016

### Keywords:

Bismuth oxyiodide

Phase transformation

Hierarchical architecture

BiOI

Bi<sub>4</sub>O<sub>5</sub>I<sub>2</sub>

Bi<sub>5</sub>O<sub>7</sub>I

## ABSTRACT

Design of three-dimensional (3D) hierarchical architectures and nano-phase-junctions are of huge significance for semiconductor photocatalysis. Herein, we report the fabrication of a series of 3D hierarchical bismuth oxyiodides via *in situ* phase transformation and phase-junction construction utilizing BiOI microspheres as self-sacrificed template through a facile calcination strategy. The multiform bismuth oxyiodides obtained at different temperatures include hierarchical BiOI, Bi<sub>4</sub>O<sub>5</sub>I<sub>2</sub>, Bi<sub>4</sub>O<sub>5</sub>I<sub>2</sub>–Bi<sub>5</sub>O<sub>7</sub>I phase-junction and Bi<sub>5</sub>O<sub>7</sub>I. These bismuth oxyiodides exhibit very distinct microstructure and band structure, and their photoabsorption was orderly tuned from 700 to 400 nm, rendering the adjustable oxidation and reduction ability of band energy levels. The photocatalytic activity of the bismuth oxyiodide series is systematically assessed by degradation of diverse antibiotic and contaminants, such as tetracycline hydrochloride, bisphenol A (BPA) and azo dye Rhodamine B (RhB). It disclosed that they present discrepant photocatalytic performance with activity order of Bi<sub>4</sub>O<sub>5</sub>I<sub>2</sub>–Bi<sub>5</sub>O<sub>7</sub>I > Bi<sub>4</sub>O<sub>5</sub>I<sub>2</sub> > Bi<sub>5</sub>O<sub>7</sub>I > BiOI, which is closely associated with the charge separation efficiency, band structure and surface area. Additionally, the photocatalytic mechanism and degradation pathway are also surveyed. The study may furnish new insights into development of novel 3D hierarchical architectures and nano-phase-junctions for heterogeneous photocatalysis.

© 2016 Elsevier B.V. All rights reserved.

## 1. Introduction

Three dimensional (3D) hierarchical architectures (e.g. hierarchical Fe<sub>2</sub>O<sub>3</sub>, SnO<sub>2</sub>, TiO<sub>2</sub> architectures), such as urchin-like, brush-like, flower-like, tree-like, dendritic and branched structures, self-assembled by the low-dimensional nanostructured building units via interactions like covalent, ionic, and hydrogen bonding as well as van der Waals forces, are an interesting class of nanomaterials and show great potentials in the fields of catalysis, lithium-ion batteries, gas sensors, sensitized solar cells, and so on [1–3].

Current environmental and energy crises fuel a booming in intensive exploration of photocatalytic materials that could purify

various contaminants and produce renewable energy through solar-energy conversion [4–6]. Hierarchical photocatalysts, owing to their interconnected and readily accessible porous networks and high specific surface areas, show strengthened light harvesting, enhanced adsorption of reactants and facilitated transport and migration of guest species to the binding sites. Therefore, synergistic effects of the diverse dimensional levels and multiform porous nanostructures can give rise to profound enhancement on the photocatalytic activity of hierarchical photocatalysts. These attractive characteristics of nanostructured hierarchical materials make them promising candidates for heterogeneous photocatalysis [7–10].

Layered bismuth-based semiconductor as a kind of emerging and promising photocatalysts have triggered considerable interests of researchers owing to their unique layered crystal configuration, which is beneficial to formation of an internal static electric field perpendicular to each layer, rendering more efficacious separation of photoinduced charge carriers [11–18]. Bismuth oxyhalides BiOX

\* Corresponding authors.

E-mail addresses: [hhw@cugb.edu.cn](mailto:hhw@cugb.edu.cn) (H. Huang), [zyh@cugb.edu.cn](mailto:zyh@cugb.edu.cn) (Y. Zhang).

(X=F, Cl, Br, I) series, as a class of main group V-VI-VII ternary oxide compounds with typical layered crystal structure composed of  $[Bi_2O_2]$  layers and double halogen atoms slabs, recently presents remarkable photocatalytic activity [19–23]. Thereinto, bismuth oxyiodides ( $Bi_xO_yI_z$ ) having relatively excellent photoabsorption in solar spectrum, have been proved to be promising photocatalytic materials for treatment of wastewater. So far,  $BiOI$ ,  $Bi_7O_9I_3$ ,  $Bi_4O_5I_2$  and  $Bi_5O_7I$  have been reported and  $BiOI$  was the one extensively studied due to its simplest atomic stoichiometric ratio and smallest band gap (1.7–1.9 eV) [24–30]. However,  $BiOI$  suffers from the high recombination of electron and holes and insufficient reduction and oxidation ability. Thus, the preparation and photocatalytic performance of the new bismuth-rich oxyiodides  $Bi_7O_9I_3$ ,  $Bi_4O_5I_2$  and  $Bi_5O_7I$  come to the notice of researchers [31–37].  $Bi_7O_9I_3$  with a brick-red color shows similar light absorption to  $BiOI$  [31], while  $Bi_4O_5I_2$  and  $Bi_5O_7I$  exhibit high photocatalytic activity by virtue of their strong oxidation and reduction ability of moderate band energy levels, which can not only decompose organic pollutant, but also convert  $CO_2$  into renewable energy [36,37]. Nevertheless, so far the reports on  $Bi_4O_5I_2$  or  $Bi_5O_7I$  were rare. In particular, to the best of our knowledge, only low-dimensional nanosheets/nanobelts of  $Bi_4O_5I_2$  or  $Bi_5O_7I$  are obtained, and 3D hierarchical architectures have not been achieved. Besides, the systematical evaluation on the photocatalytic performance of these agnate bismuth oxyiodides is imperative to provide more insights and understanding. Given these, the controllable synthesis of 3D hierarchical architectures of bismuth oxyiodide photocatalysts is appealing and highly anticipated.

In this work, we first prepared  $BiOI$  3D hierarchical microsphere by a simple ethylene-glycol assisted room-temperature precipitation process, and then  $BiOI$  3D hierarchical microsphere as self-template were *in situ* calcinated to be converted into diverse 3D hierarchical architectures at different temperature, including  $Bi_4O_5I_2$ ,  $Bi_4O_5I_2$ - $Bi_5O_7I$  phase-junction and  $Bi_5O_7I$ . Their microstructure, optical absorption and band structure are carefully investigated and compared. The photocatalysis performance of the series of bismuth oxyiodide is systematically assessed by degrading various antibiotic and contaminants, such as tetracycline hydrochloride, bisphenol A (BPA) and azo dye Rhodamine B (RhB). The results demonstrated that they show different photocatalytic activity which is closely related to the charge separation efficiency, surface area and band structure. Our work may shed new light on development of novel 3D hierarchical architectures and nano-phase-junction by facile *in situ* treatment.

## 2. Experimental section

### 2.1. Synthesis

The chemicals used in this work are all in analytical grade without further purification.  $BiOI$  microspheres are first prepared by the ethylene glycol (EG)-assisted *in situ* hydrolysis method at room temperature according to our previously reported work [25].  $Bi(NO_3)_3 \cdot 5H_2O$  (1 mmol) was first dissolved into 25 ml of deionized water under vigorously stirring, then it was dropwise added into 25 ml of  $KI$  (1 mmol) water solution resulting in red-colored precipitation. The suspension was kept stirring for 3 h. Afterwards, the solids were filtrated and washed repeatedly with deionized water and ethanol, and dried at 80 °C for 10 h to collect  $BiOI$  microspheres.

$Bi_4O_5I_2$ ,  $Bi_5O_7I$ , and  $Bi_4O_5I_2$ - $Bi_5O_7I$  composites are prepared by an *in situ* calcination method using  $BiOI$  as precursors. Based on the TG-DTA curve of  $BiOI$ , the calcination temperatures are set as 350 °C, 380 °C, 410 °C, 440 °C, 470 °C and 500 °C, respectively. The  $BiOI$  precursors are put in an agate corundum crucible and heated in a muffle furnace at the above temperatures at a heating rate of

3 °C/min. When the furnace was finally cooled to room temperature, the samples obtained at different temperatures are collected and to be measured.

### 2.2. Characterization

X-ray powder diffraction (XRD) was carried out on a D8 Advance X-ray diffractometer (Bruker AXS, Germany) with  $Cu K\alpha$  radiation ( $\lambda = 1.5418 \text{ \AA}$ ). The surface element state is inspected on a Perkin-Elmer PHI 5000C X-ray photoelectron spectroscopy (XPS). Scanning electron microscopy (SEM) and transmission electron microscopy (TEM) are conducted to obtain the microstructure and morphology information on a S-4800 and JEM-2100F microscopy, respectively. A Varian 710-ES (Varian, Shanghai, China) inductively coupled plasma optical emission spectrometer (ICP-OES) with Sepex Certiprep standards was used to analyze the related elements of samples. A UV-vis spectrophotometer (Varian Cary 5000) was employed to record the UV-vis diffuse reflectance spectra (DRS) of samples. The  $N_2$  adsorption-desorption isotherms and specific surface area were measured by an automated gas sorption analyzer (Autosorb-iQ-2MP, Quantachrome, USA). Thermogravimetric (TG) and differential thermal analysis (DTA) curves of  $BiOI$  are collected on a Labsys TGDTA16 (SETARAM) thermal analyzer.

### 2.3. Photocatalytic evaluation

The photocatalytic activity of samples are assessed through degradation of tetracycline hydrochloride (10 mg/L), bisphenol A (BPA, 10 mg/L) and Rhodamine B (RhB, 0.02 mM) with visible light irradiation (500 W Xe lamp,  $\lambda > 420 \text{ nm}$ ). The photodegradation experiments are performed by the following procedures: Photocatalyst powder (50 mg) was put into the quartz tube that containing 50 ml of the above tetracycline hydrochloride/BPA/RhB solutions and totally dispersed under strong ultrasonic. First, it was allowed to achieve an adsorption-desorption equilibrium between pollutants and catalyst in darkness. Then, they are exposed to light, and the supernatant liquid was sampled at certain intervals. The concentration change of solutions is determined by measuring the change of the characteristic absorbance bands of the contaminants on a Cary 5000 UV-vis spectrophotometry.

### 2.4. Active species trapping experiment

The active species that may be produced in the photocatalytic process are inspected by active species trapping experiment. Benzoquinone (BQ), disodium ethylenediaminetetraac-eteate (EDTA-2Na) and isopropanol (IPA) are added in the quartz tube of the photodegradation experiment to inspected superoxide radical ( $\bullet O_2^-$ ), hole ( $h^+$ ) and hydroxyl radical ( $\bullet OH$ ), respectively.

### 2.5. Photocatalytic degradation intermediates identification

The photodegradation intermediates in BPA degradation were separated and recorded by a high-performance liquid chromatography (HPLC, Lumtech). The Venusil XBP-C18 (250 × 4.6 mm i. d., 5  $\mu\text{m}$ ) reversed phase column was used. The mobile phase is the mixture of water and acetonitrile with a ratio of 35:65 (v/v). The flow rate was kept as 1.0 ml/min, and 10  $\mu\text{l}$  of solution was injected to be analyzed. The column was maintained at 30 °C during the sample analysis.

### 2.6. Photoelectrochemical measurements

The photoelectrochemical measurements were all carried out in a three-electrode quartz cells on an electrochemical system (CHI-660E, China). The reference electrode is a saturated calomel

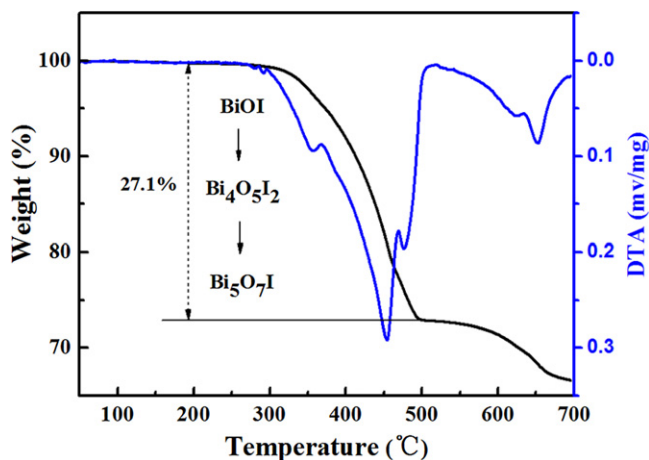


Fig. 1. TG-DTA curves of BiOI.

electrode (SCE), and the counter electrode is the platinum wires. The working electrode is the sample films coated on the ITO glasses. The electrolyte is 0.1 M Na<sub>2</sub>SO<sub>4</sub> solution. A 300 W Xe lamp with 420 nm filters was used as the light source.

### 3. Results and discussion

#### 3.1. Phase-transformation and structure investigation

TG-DTA measurement was conducted to investigate the phase transformation of BiOI. As shown in Fig. 1, there are mainly four endothermic peaks from room temperature to 700 °C during the calcination process, which occurred at 350 °C, 450 °C, 480 °C and 660 °C. Accordingly, the calcination temperatures are set as 350 °C, 380 °C, 410 °C, 440 °C, 470 °C, 500 °C, 530 °C and 560 °C, respectively, and the phase composition of corresponding samples is studied by XRD. In the TG-DTA curve, the first peak appeared at 350 °C sample corresponds to the phase transition from BiOI to Bi<sub>4</sub>O<sub>5</sub>I<sub>2</sub>. As confirmed by the XRD patterns (Fig. 2a), the (102) diffraction peak of BiOI (ICSD #24610) gradually shifts to a lower 2θ angle from 350 °C to 410 °C, and BiOI totally turns to be Bi<sub>4</sub>O<sub>5</sub>I<sub>2</sub> (ICSD #412590) till it was heated at 410 °C. The sample at 380 °C may be attributed to a BiOI phase with I vacancy [31]. When the calcination temperature further increases, Bi<sub>4</sub>O<sub>5</sub>I<sub>2</sub> starts to decompose. In addition to the Bi<sub>4</sub>O<sub>5</sub>I<sub>2</sub> diffraction peaks, the (314) diffraction peak of Bi<sub>5</sub>O<sub>7</sub>I (ICSD #411666) emerges in the XRD pattern of 440 °C sample, and all the Bi<sub>5</sub>O<sub>7</sub>I characteristic peaks are found in the 470 °C sample besides a slight trace of Bi<sub>4</sub>O<sub>5</sub>I<sub>2</sub>, demonstrating that calcinated products of BiOI at 440 °C and 470 °C are the composite of Bi<sub>4</sub>O<sub>5</sub>I<sub>2</sub> and Bi<sub>5</sub>O<sub>7</sub>I. When the calcination temperature increases to 500 °C, BiOI was completely changed into Bi<sub>5</sub>O<sub>7</sub>I (Fig. 2b). The weight loss from room temperature to 500 °C is 27.1% (Fig. 1), which is in good agreement with the calculated value from BiOI to Bi<sub>5</sub>O<sub>7</sub>I. As further heated to 530 °C or 560 °C, other new peaks appear in the XRD pattern (Fig. 2c), which is attributed to the decomposition of Bi<sub>5</sub>O<sub>7</sub>I into Bi<sub>2</sub>O<sub>3</sub>, corresponding to the weight loss after 500 °C in TG curve. As the samples are melt and hard to be separated from the crucible after 500 °C (like, 530 °C or 560 °C), we only focus on the study of the samples obtained before 500 °C (350 °C, 380 °C, 410 °C, 440 °C, 470 °C and 500 °C).

Elements analysis was conducted to confirm different phases and reveal the real composition of calcinated products from BiOI. It can be seen from Table S1 that the atomic ratios of related elements correspond well to their samples that are obtained by XRD pattern.

XPS analysis is used to survey the coordination environment of bismuth and iodine elements in the bismuth iodide compounds.

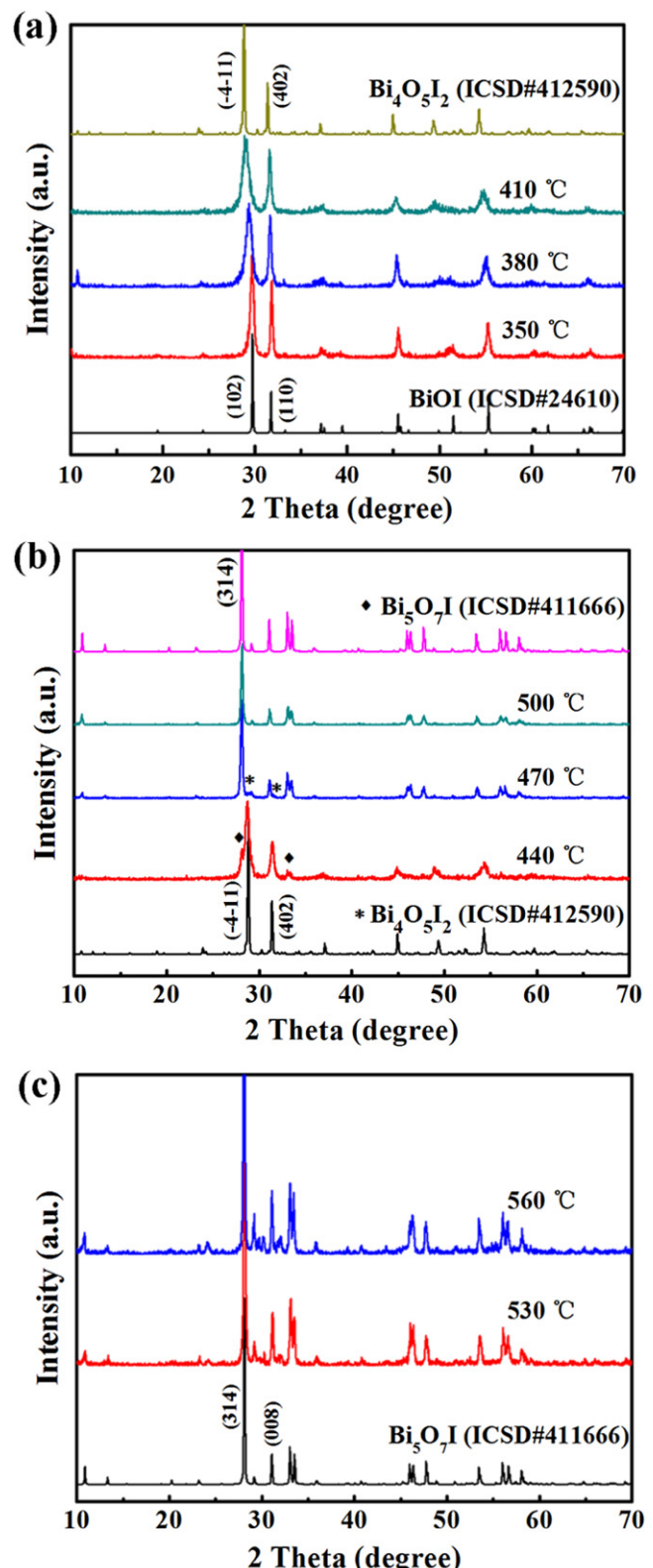


Fig. 2. XRD patterns of calcinated products of BiOI microsphere at different temperatures.

For 350 °C sample, the two Bi<sup>3+</sup> characteristic peaks at 164.7 eV and 159.3 eV are ascribed to the Bi 4f<sub>5/2</sub> and Bi 4f<sub>7/2</sub> of BiOI, respectively (Fig. 3 a) [36]. In contrast, these peaks of 410 °C (Bi<sub>4</sub>O<sub>5</sub>I<sub>2</sub>) and 500 °C (Bi<sub>5</sub>O<sub>7</sub>I) show an obvious shift to low binding energies. As the oxygen atom possesses a larger electronegativity than iodine atom, the

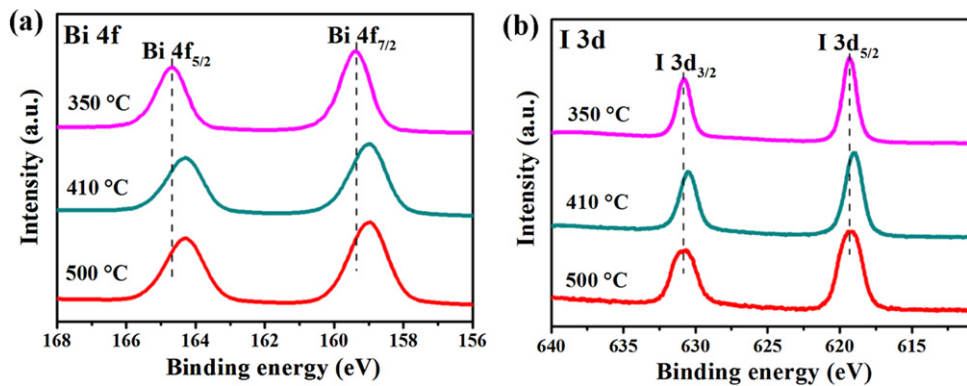


Fig. 3. XPS spectra of BiOI calcinated products at 350 °C, 410 °C and 500 °C: (a) Bi 4f and (b) I 3d.

decrease of Bi<sup>3+</sup> binding energies indicate that Bi<sup>3+</sup> are coordinated with more oxygen atoms instead of iodine atoms, consistent with phase transformation from BiOI to Bi<sub>4</sub>O<sub>5</sub>I<sub>2</sub> to Bi<sub>5</sub>O<sub>7</sub>I [31]. Besides, the binding energies of I 3d<sub>3/2</sub> and I 3d<sub>5/2</sub> at 631.2 eV and 619.2 eV undergo little change (Fig. 3b), which is due to their steady chemical coordination with bismuth atoms.

The evolution on microstructure and morphology from BiOI to Bi<sub>5</sub>O<sub>7</sub>I are studied by SEM. BiOI prepared by EG-assisted precipitation method shows uniform hierarchical microsphere morphology (Fig. 4a, diameter is about 1  $\mu$ m), which is assembled by large amounts of nanosheets with average size of 100 nm. As BiOI was calcinated at 350 °C or 380 °C, it rapidly grows into more uni-

formly square nanosheets with higher crystallinity and a larger size of 400–600 nm, and the as-constituted microsphere is approximately 3  $\mu$ m in diameter (Fig. 4b, c, g and h). When the calcination temperature increases to 410 °C, the hierarchical microspheres are composed of irregular nanoparticles and the size of did not further increase (Fig. 4d and i), which indicates that Bi<sub>4</sub>O<sub>5</sub>I<sub>2</sub> may have a higher specific surface area than BiOI. It is notable to observe that the sample synthesized at 440 °C present a mixed-phase structure constituted by Bi<sub>4</sub>O<sub>5</sub>I<sub>2</sub> nanoparticles and sandwich-like nanosheets (Fig. 4e and j). According to the XRD result, the sandwich-like nanosheets are Bi<sub>5</sub>O<sub>7</sub>I. As confirmed by the SEM images (Fig. 4f), the 500 °C sample (Bi<sub>5</sub>O<sub>7</sub>I) exhibits a microsphere structure

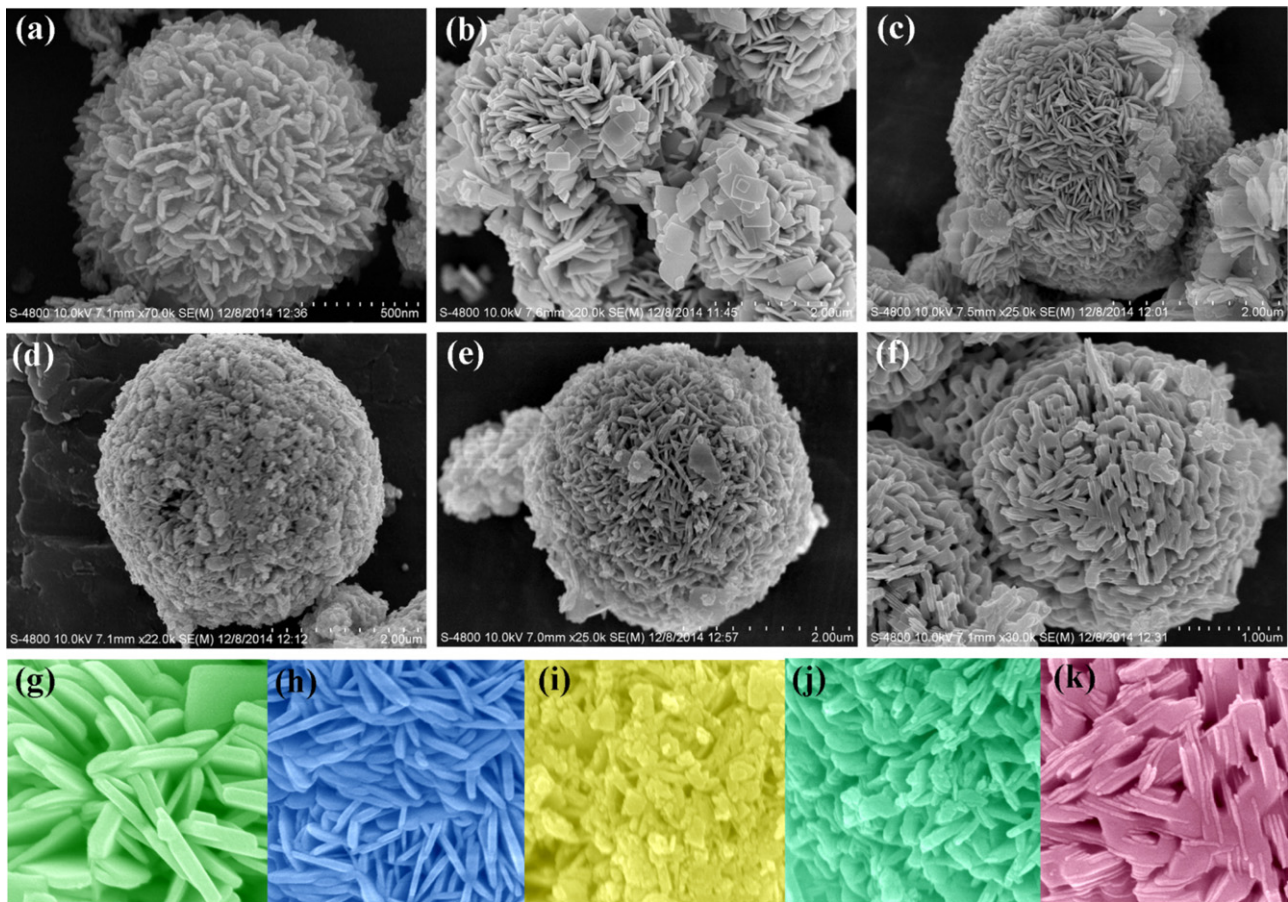


Fig. 4. SEM images of BiOI microsphere (a) and calcinated products at 350 °C (b and g), 380 °C (c and h), 410 °C (d and i), 440 °C (e and j) and 500 °C (f and k).

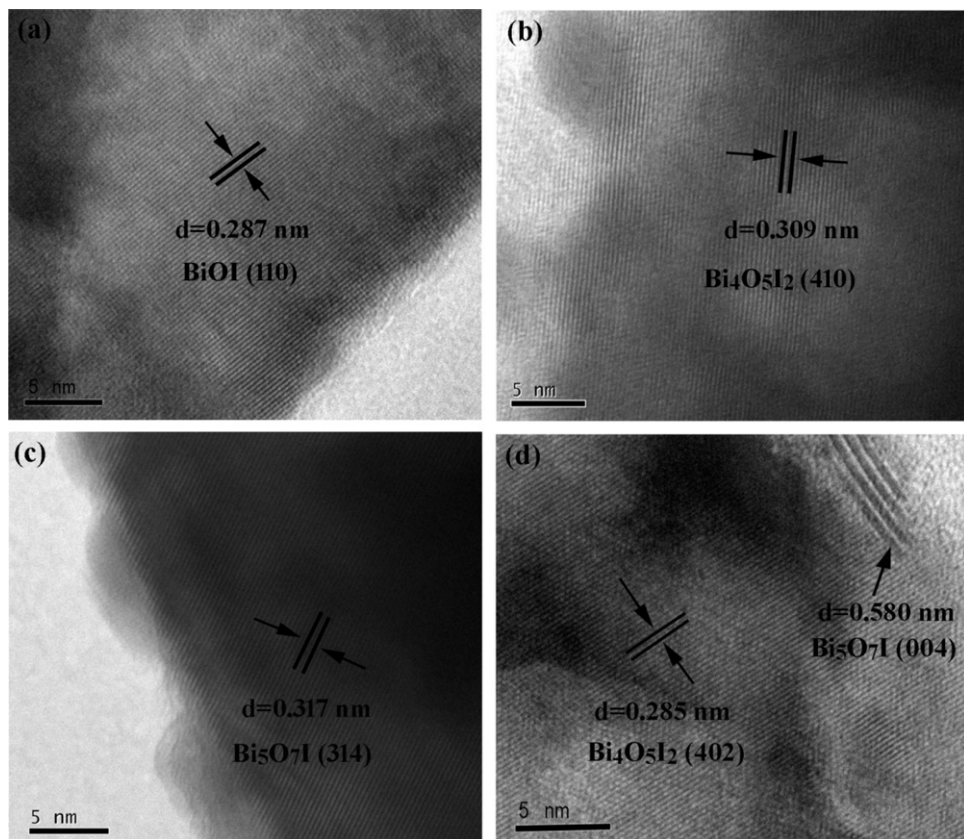
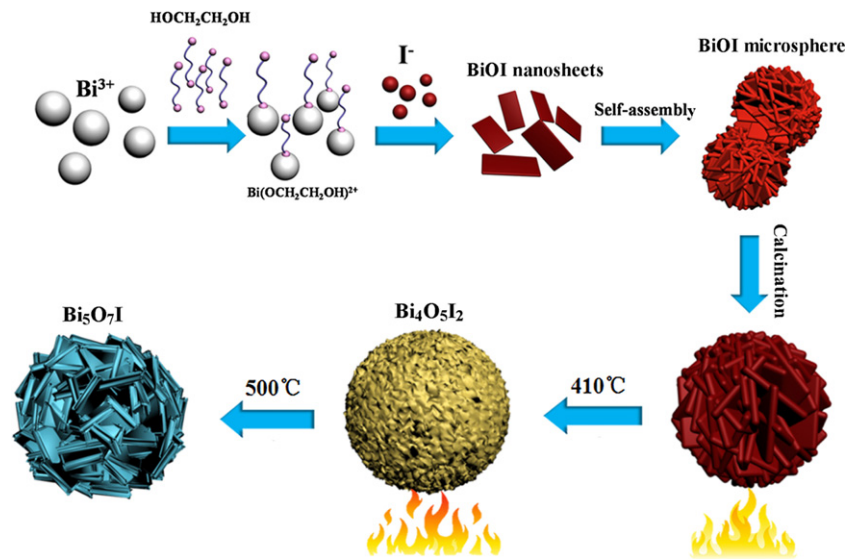


Fig. 5. HRTEM images of calcinated BiOI at (a) 350 °C, (b) 410 °C, (c) 500 °C and (d) 440 °C.



Scheme 1. Formation diagram of the hierarchical architectures of BiOI, Bi<sub>4</sub>O<sub>5</sub>I<sub>2</sub>, Bi<sub>4</sub>O<sub>5</sub>I<sub>2</sub>-Bi<sub>5</sub>O<sub>7</sub>I composite and Bi<sub>5</sub>O<sub>7</sub>I.

consisting of unique sandwich-like nanosheets. It also verified that the 440 °C sample is the composite Bi<sub>4</sub>O<sub>5</sub>I<sub>2</sub> and Bi<sub>5</sub>O<sub>7</sub>I. Besides, the lower dimension SEM images of calcinated BiOI products are also provided in Fig. S1a-f, which further confirms the uniformly spherical structures of these samples.

A more visually schematic illustration of the phase transformation and morphology evolution from BiOI to Bi<sub>5</sub>O<sub>7</sub>I is depicted in Scheme 1. First, the Bi<sup>3+</sup> reacts with ethylene glycol to form a homogeneous Bi(OCH<sub>2</sub>CH<sub>2</sub>OH)<sup>2+</sup> solution, which transforms into

BiOI nanoplates after reacting with KI, and then the BiOI nanoplates are self-assembled into BiOI microspheres for the sake of reducing the surface energy. This process has been proposed in the previous work [10]. When BiOI microspheres were calcinated at 350 °C or 380 °C, the BiOI crystallization phase keeps unchanged only the microsphere size increased. With raising the calcination temperature to 410 °C, BiOI turns to be Bi<sub>4</sub>O<sub>5</sub>I<sub>2</sub>. The calcination product is the mixture of Bi<sub>4</sub>O<sub>5</sub>I<sub>2</sub> and Bi<sub>5</sub>O<sub>7</sub>I at 440 °C and 470 °C, and totally transforms into Bi<sub>5</sub>O<sub>7</sub>I at 500 °C.

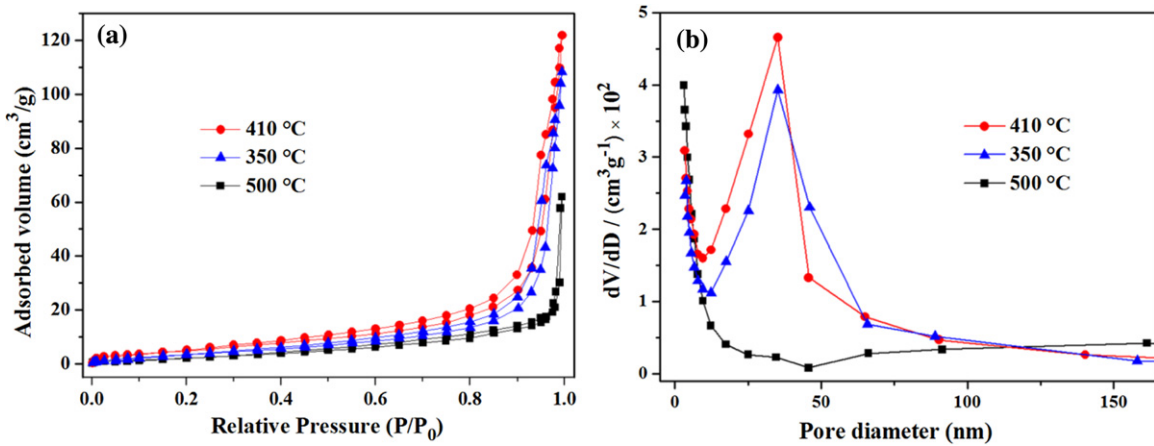


Fig. 6.  $\text{N}_2$  adsorption-desorption isotherms (a) and the corresponding pore size distribution curves (b) of calcinated  $\text{BiOI}$  at  $350^\circ\text{C}$ ,  $410^\circ\text{C}$  and  $500^\circ\text{C}$ .

HRTEM was conducted herein to corroborate the phase transformation during the calcination process. As shown in Fig. 5a, one can see a set of clear lattice fringes for the  $350^\circ\text{C}$  sample with a spacing of  $0.287\text{ nm}$ , which corresponds to the  $(110)$  plane of  $\text{BiOI}$ . This indicates that the main exposed facet of  $\text{BiOI}$  is  $\{001\}$  facet. For the  $410^\circ\text{C}$  sample (Fig. 5b), the interplanar spacing of lattice fringe is  $0.309\text{ nm}$ , which can be assigned to the  $(410)$  plane of  $\text{Bi}_4\text{O}_5\text{I}_2$ . Fig. 5c displays a set of uniform lattice fringe of  $500^\circ\text{C}$  sample. An interplanar spacing of  $0.371\text{ nm}$  was observed, matching well with the  $(314)$  plane of  $\text{Bi}_5\text{O}_7\text{I}$ . Regarding the  $440^\circ\text{C}$  sample, one can obviously see two sets of distinct lattice fringes in the visual field. The lattice fringe with an interplanar spacing of  $0.580\text{ nm}$  corresponds well to the  $(004)$  plane of  $\text{Bi}_5\text{O}_7\text{I}$ , and the other one with lattice spacing of  $0.285\text{ nm}$  is indexed into the  $(402)$  plane of  $\text{Bi}_4\text{O}_5\text{I}_2$ . It demonstrates that the co-existence of  $\text{Bi}_5\text{O}_7\text{I}$  and  $\text{Bi}_4\text{O}_5\text{I}_2$  in the  $440^\circ\text{C}$  sample. The HRTEM result affirmed the phase transformation from  $\text{BiOI}$  to  $\text{Bi}_5\text{O}_7\text{I}$  during the calcination process, and is in good line with the XRD result.

As the sample obtained at different temperature has distinct morphology, the products are investigated by adsorption-desorption method. Fig. 6 shows the nitrogen adsorption-desorption isotherms and pore size distribution curves of calcinated  $\text{BiOI}$  products at  $350^\circ\text{C}$  ( $\text{BiOI}$ ),  $410^\circ\text{C}$  ( $\text{Bi}_4\text{O}_5\text{I}_2$ ) and  $500^\circ\text{C}$  ( $\text{Bi}_5\text{O}_7\text{I}$ ).  $\text{BiOI}$  and  $\text{Bi}_4\text{O}_5\text{I}_2$  exhibit type IV isotherms according to BDDT classification (Fig. 6a), which signifies the presence of mesopores. The hysteresis loop belongs to type H3 in IUPAC classification, indicating that the pores are resulted from the aggregations of the nanosheets. The pore size range of  $\text{BiOI}$  and  $\text{Bi}_4\text{O}_5\text{I}_2$  is  $10\text{--}60\text{ nm}$ , and their main pore sizes are  $35\text{ nm}$  (Fig. 6b). In contrast, the adsorption isotherms for  $\text{Bi}_5\text{O}_7\text{I}$  are specified as type II (Fig. 6a), reflecting the characteristic of nonporous or macroporous materials, which is confirmed by its pore size distribution (Fig. 6b). The BET specific surface areas of  $\text{BiOI}$ ,  $\text{Bi}_4\text{O}_5\text{I}_2$  and  $\text{Bi}_5\text{O}_7\text{I}$  are  $20.7$ ,  $22.6$  and  $9.2\text{ m}^2/\text{g}$ , respectively. The reduced pores and surface area of  $\text{Bi}_5\text{O}_7\text{I}$  compared with  $\text{BiOI}$  and  $\text{Bi}_4\text{O}_5\text{I}_2$  is mainly due to the higher calcination temperature, which results in the more compact assembly structure.

### 3.2. Optical absorption and band gap analyses

In addition to the microstructure evolution, the phase transformation gives rise to the drastic change in optical property, which is investigated by diffuse reflectance spectra (DRS). As displayed in Fig. 7a, the absorption edge of  $\text{BiOI}$  is approximately situated at  $665\text{ nm}$ . It is significant to see that the absorption edge of samples orderly blue-shifts from  $665\text{ nm}$  to  $420\text{ nm}$  as the calcination temperature increases from  $350^\circ\text{C}$  to

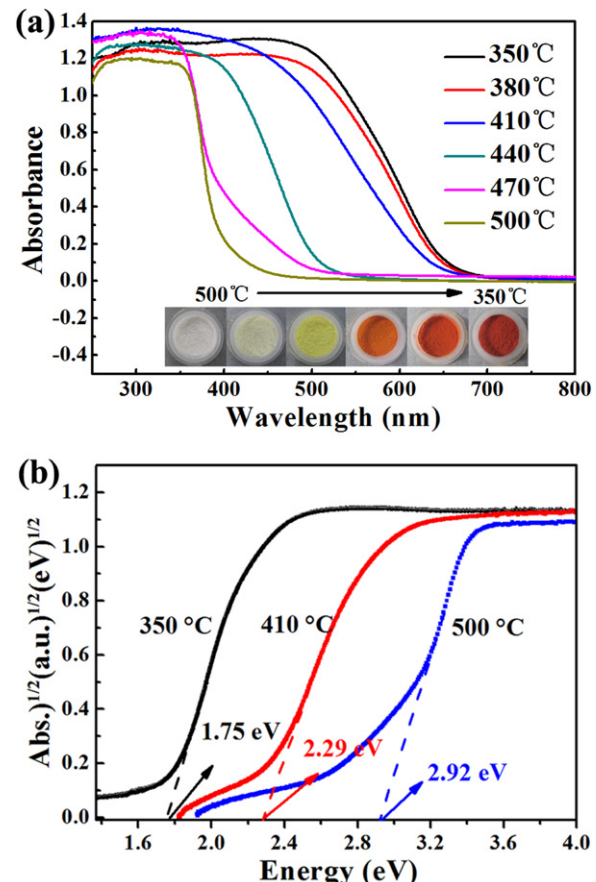
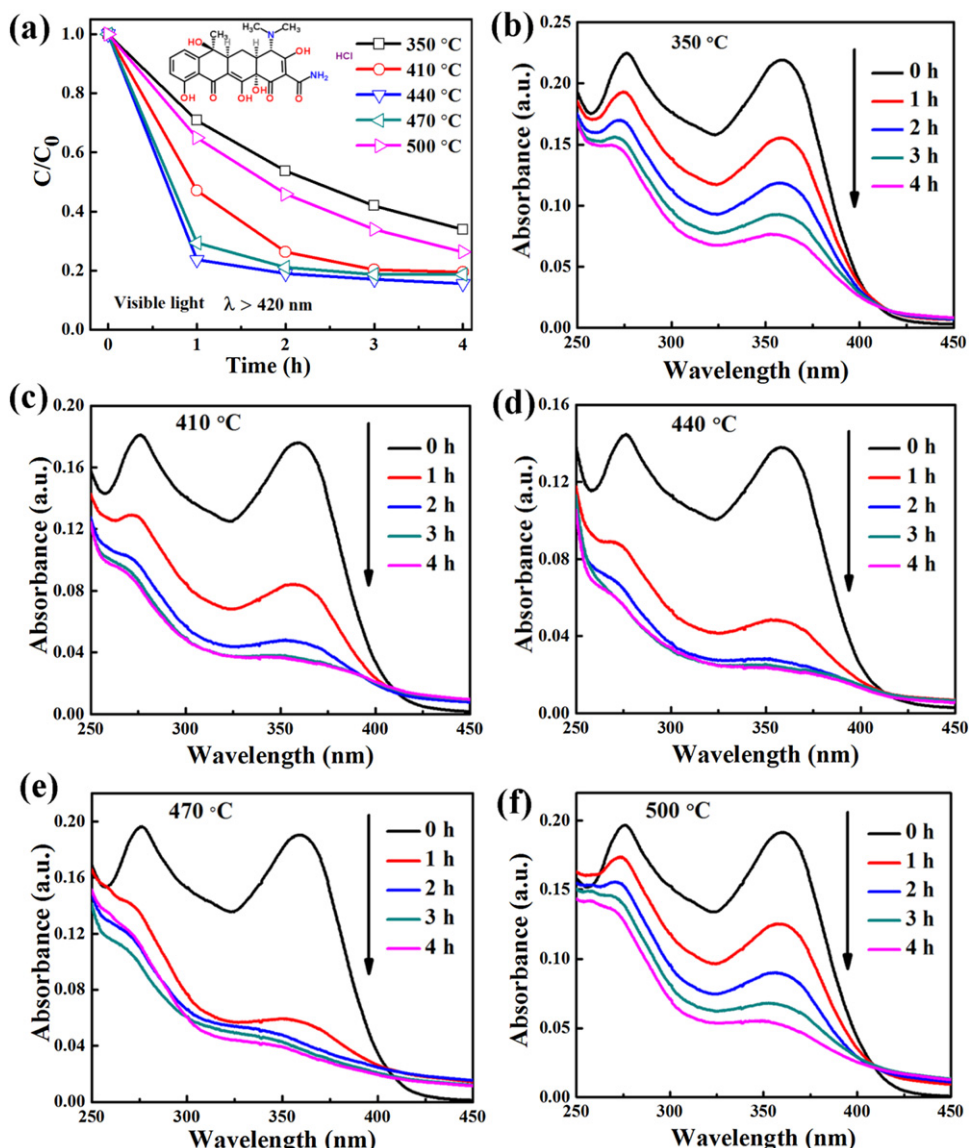
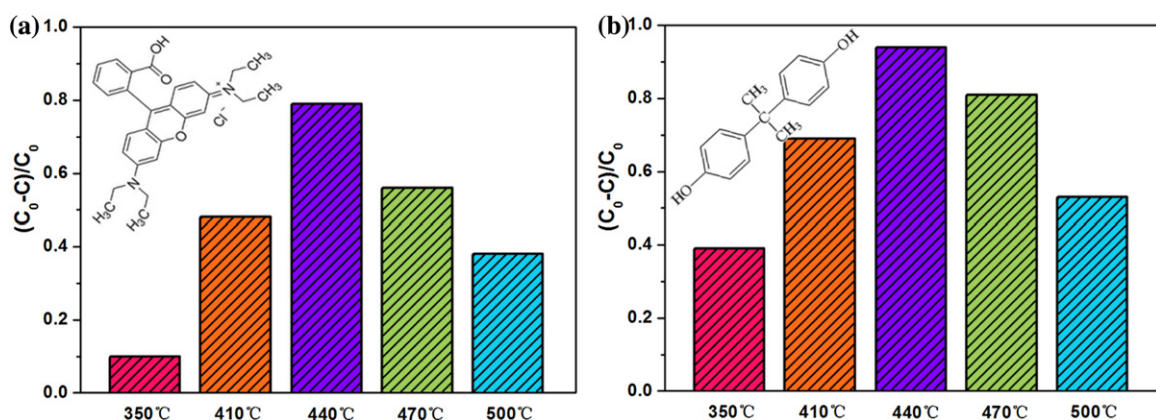


Fig. 7. (a) UV-vis diffuse reflectance spectra of calcinated  $\text{BiOI}$  at different temperatures and the corresponding color of samples (inset). (b) Band gaps of calcinated  $\text{BiOI}$  at  $350^\circ\text{C}$ ,  $410^\circ\text{C}$  and  $500^\circ\text{C}$ .

$500^\circ\text{C}$ . Accordingly, they display a color change ranging from brick red to orange, yellow, light yellow and white (inset of Fig. 7a). It revealed the gradual enlargement of band gap and further confirmed the phase transformation from  $\text{BiOI}$  to  $\text{Bi}_4\text{O}_5\text{I}_2$ ,  $\text{Bi}_4\text{O}_5\text{I}_2\text{-}\text{Bi}_5\text{O}_7\text{I}$  and  $\text{Bi}_5\text{O}_7\text{I}$ . The optical band gaps of single semiconductor can be determined by DRS [38]. As displayed in the plots of  $(\alpha h\nu)^{1/2}$  versus  $(h\nu)$  in Fig. 7b, the band gaps of sample at  $350^\circ\text{C}$  ( $\text{BiOI}$ ),  $410^\circ\text{C}$  ( $\text{Bi}_4\text{O}_5\text{I}_2$ ) and  $500^\circ\text{C}$  ( $\text{Bi}_5\text{O}_7\text{I}$ ) are calculated to be  $1.75\text{ eV}$ ,  $2.29\text{ eV}$  and  $2.92\text{ eV}$ , respectively. The difference in band gap and band structure may have a large impact on the



**Fig. 8.** (a) Photodegradation curves of tetracycline hydrochloride over calcinated BiOI at different temperatures under visible light irradiation ( $\lambda > 420$  nm) and (b–f) the corresponding UV-vis absorption spectra.



**Fig. 9.** (a) Photodegradation efficiency of (a) RhB and (b) BPA over calcinated BiOI at different temperatures under visible light irradiation ( $\lambda > 420$  nm).

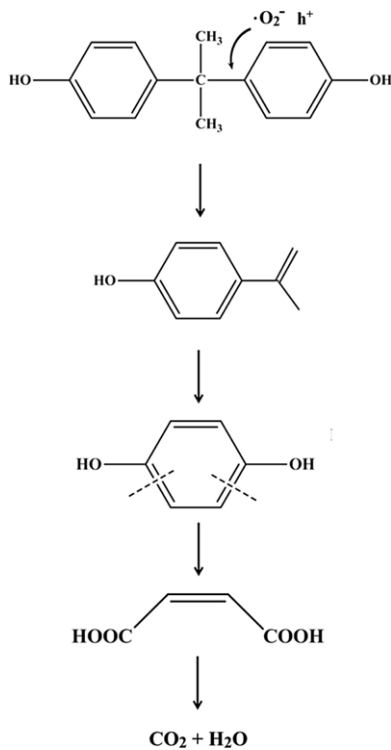


**Fig. 10.** Proposed BPA degradation pathway by  $\text{Bi}_4\text{O}_5\text{I}_2\text{-}\text{Bi}_5\text{O}_7\text{I}$  heterojunction under visible light irradiation.

photocatalytic performance, which will be discussed in the following.

### 3.3. Photocatalytic activity investigation

#### 3.3.1. Photodegradation of tetracycline hydrochloride

In order to inspect the photocatalytic performance of the series of calcination samples, tetracycline hydrochloride that could bring about antibiotic-resistant pathogens development is chose as the probing target under visible light irradiation ( $\lambda > 420 \text{ nm}$ ). As seen from Fig. 8a, the photodegradation rates of these samples after 4 h irradiation tend to show smaller gaps due to low concentration of the surviving tetracycline hydrochloride, and the photodegradation efficiencies at the initial period is more reasonable to be selected to evaluate their activity difference of samples. It is easy to note that the photocatalytic activity order of the samples is  $440^\circ\text{C}$  ( $\text{Bi}_4\text{O}_5\text{I}_2\text{-}\text{Bi}_5\text{O}_7\text{I}$ )  $>$   $470^\circ\text{C}$  ( $\text{Bi}_4\text{O}_5\text{I}_2\text{-}\text{Bi}_5\text{O}_7\text{I}$ )  $>$   $410^\circ\text{C}$  ( $\text{Bi}_4\text{O}_5\text{I}_2$ )  $>$   $500^\circ\text{C}$  ( $\text{Bi}_5\text{O}_7\text{I}$ )  $>$   $350^\circ\text{C}$  ( $\text{BiOI}$ ). With 1 h illumination, the photodecomposition efficiencies for  $350^\circ\text{C}$ ,  $410^\circ\text{C}$ ,  $440^\circ\text{C}$ ,  $470^\circ\text{C}$

and  $500^\circ\text{C}$  samples are 28%, 53%, 78%, 72% and 35%, respectively. Evidently, the two  $\text{Bi}_4\text{O}_5\text{I}_2\text{-}\text{Bi}_5\text{O}_7\text{I}$  composites show the best photocatalytic activity, and the optimal photocatalytic activity obtained at  $440^\circ\text{C}$  composite sample ( $\text{Bi}_4\text{O}_5\text{I}_2\text{-}\text{Bi}_5\text{O}_7\text{I}$ ) is almost 3 times that of  $350^\circ\text{C}$  product ( $\text{BiOI}$ ). Fig. 8b–f presents the time-resolved absorption spectra of tetracycline hydrochloride catalyzed by these samples. The characteristic absorbance of tetracycline hydrochloride at 270 nm and 350 nm gradually decreases with prolonging the irradiation time for all the samples, and the decrease level corresponds well to their photodegradation activity order. It is obvious to see that  $440^\circ\text{C}$  sample ( $\text{Bi}_4\text{O}_5\text{I}_2\text{-}\text{Bi}_5\text{O}_7\text{I}$ ) exhibits the largest decline in the absorption peaks. The difference in photocatalytic activity of these samples will be discussed later.

#### 3.3.2. Photodegradation of Rhodamine B and Bisphenol A

To further confirm the photooxidation ability of this series of samples, azo dye model Rhodamine B (RhB) and a typical endocrine-disrupting chemical bisphenol A (BPA) which can cause reproductive abnormalities are utilized for the photodegradation experiment. Similar to the above tetracycline hydrochloride degradation result, the two  $\text{Bi}_4\text{O}_5\text{I}_2\text{-}\text{Bi}_5\text{O}_7\text{I}$  composites also present much superior photodegradation abilities than other samples for RhB and BPA degradation, as seen from Fig. 9a and b. Under 4 h visible light irradiation, the largest photodegradation efficiencies of RhB and BPA can achieve 79% and 94%, respectively, by the  $440^\circ\text{C}$  composite sample ( $\text{Bi}_4\text{O}_5\text{I}_2\text{-}\text{Bi}_5\text{O}_7\text{I}$ ). With respect to the pristine samples,  $410^\circ\text{C}$  sample ( $\text{Bi}_4\text{O}_5\text{I}_2$ ) exhibits the fastest degradation rate, followed by  $500^\circ\text{C}$  sample ( $\text{Bi}_5\text{O}_7\text{I}$ ), and the  $350^\circ\text{C}$  product ( $\text{BiOI}$ ) is the worst performer. It is apparent that the activity order accords strictly with that of the above tetracycline hydrochloride deterioration, revealing that these bismuth iodide photocatalysts have nonselective photooxidizing ability that can destroy various industrial contaminants and antibiotics.

#### 3.3.3. Photocatalytic degradation mechanism

Photocatalytic degradation mechanism of contaminants over  $400^\circ\text{C}$   $\text{Bi}_4\text{O}_5\text{I}_2\text{-}\text{Bi}_5\text{O}_7\text{I}$  sample was investigated by active species trapping experiment [26]. Disodium ethylenediaminetetraacetate (EDTA-2Na), benzoquinone (BQ), and isopropanol (IPA) are introduced as the scavengers of hole ( $\text{h}^+$ ), superoxide radical ( $\text{·O}_2^-$ ) and hydroxyl radical ( $\text{·OH}$ ), respectively. It can be seen from Fig. S2 that the degradation efficiency of tetracycline hydrochloride is significantly retarded by adding BQ and moderately slowed down by the addition of EDTA-2Na. It indicates that  $\text{·O}_2^-$  takes a dominant part in the pollutant decomposition process and  $\text{h}^+$  plays a second role.

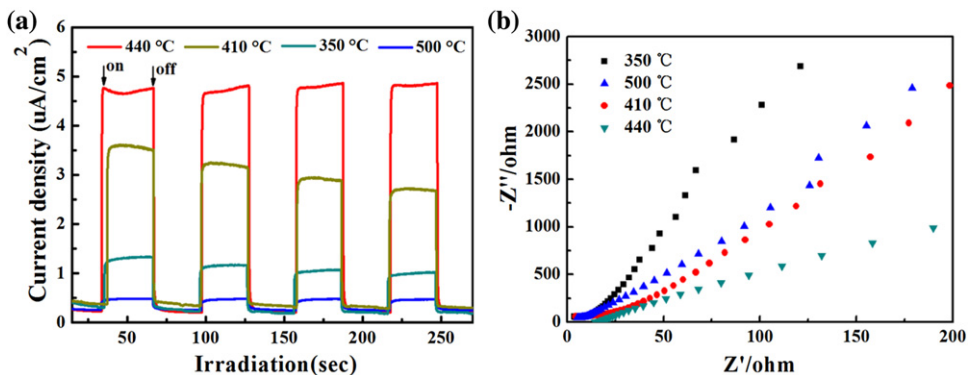


**Fig. 11.** (a) Transient photocurrent responses and (b) EIS Nyquist plots of calcinated  $\text{BiOI}$  at  $350^\circ\text{C}$ ,  $410^\circ\text{C}$ ,  $440^\circ\text{C}$  and  $500^\circ\text{C}$  under visible light illumination ( $\lambda > 420 \text{ nm}$ ).

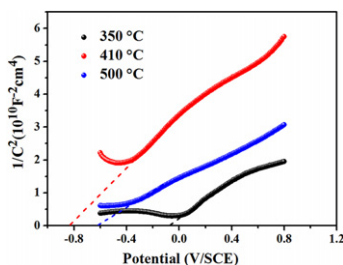


**Fig. 12.** Mott-Schottky curves of calcined products of BiOI at 350 °C, 410 °C and 500 °C.

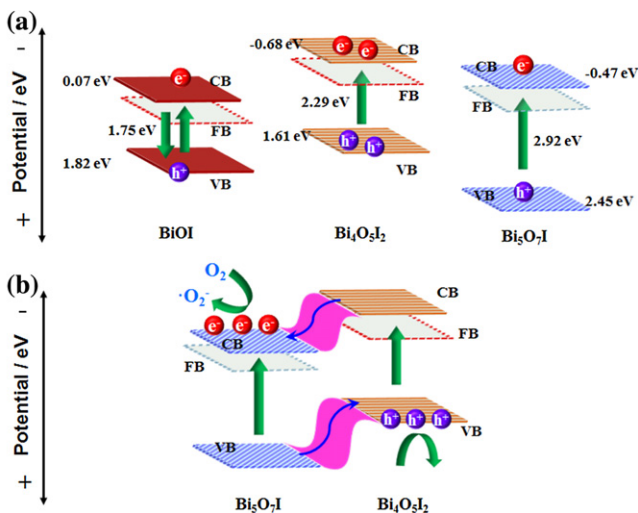


**Fig. 13.** Schematic diagrams of charge separation and transfer process for (a) the single photocatalyst of BiOI, Bi<sub>4</sub>O<sub>5</sub>I<sub>2</sub> and Bi<sub>5</sub>O<sub>7</sub>I and (b) Bi<sub>4</sub>O<sub>5</sub>I<sub>2</sub>-Bi<sub>5</sub>O<sub>7</sub>I phase junction.

### 3.3.4. Photocatalytic degradation intermediates and pathway

To further survey the contaminant degradation pathway catalyzed by the Bi<sub>4</sub>O<sub>5</sub>I<sub>2</sub>-Bi<sub>5</sub>O<sub>7</sub>I composite, the intermediates generated in the photocatalytic reaction were analyzed by HPLC employing BPA decomposition process as a representative. As presented in Fig. S3, the characteristic peak of BPA was reduced and new peaks emerged in the photodegradation process, which discloses the efficient decomposition of BPA and the generation of transformation intermediates. The main intermediates with peak appearing at 5.514 and 5.926 min are determined to be hydroquinone and maleic acid, respectively, consistent with the literature [39].

A possible BPA degradation pathway was thus proposed as displayed in Fig. 10. The photogenerated superoxide radical (•O<sub>2</sub><sup>-</sup>) and hole (h<sup>+</sup>) are the two dominating active oxygen species in the BPA degradation process over Bi<sub>4</sub>O<sub>5</sub>I<sub>2</sub>-Bi<sub>5</sub>O<sub>7</sub>I. It can be deduced that •O<sub>2</sub><sup>-</sup> and h<sup>+</sup> firstly attacked and broke the C-C bond in the long chain of BPA, and produced 4-Isopropenylphenol. Then, demethylation and hydroxylation reactions occurred, resulting in the generation of hydroquinone. As the reaction continues, the aromatic rings of hydroquinone were split and maleic acid was generated through ring-rupturing reaction. It can be concluded that these intermediates were gradually oxidized and converted into small molecules, like formic and acetic acids, and subsequently resulted in the complete mineralization of BPA [39].

### 3.3.5. Stability of photocatalyst

The recyclability and stability of the as-obtained 440 °C Bi<sub>4</sub>O<sub>5</sub>I<sub>2</sub>-Bi<sub>5</sub>O<sub>7</sub>I catalyst for tetracycline hydrochloride degradation are studied by conducting cycling experiment. As shown in Fig. S4,

the photocatalytic performance of the 440 °C Bi<sub>4</sub>O<sub>5</sub>I<sub>2</sub>-Bi<sub>5</sub>O<sub>7</sub>I was well maintained and no obvious activity decrease for the tetracycline hydrochloride degradation can be seen after four times of cycles, and the samples can be easily separated and collected by centrifugation. It revealed the Bi<sub>4</sub>O<sub>5</sub>I<sub>2</sub>-Bi<sub>5</sub>O<sub>7</sub>I photocatalyst has a high stability and good recyclability in degradation of contaminants, which is important for practical applications.

### 3.4. Analysis on the difference of photocatalytic activity

The photocatalytic performance is associated with many factors, such as charge separation, band structure, surface area, etc. Charge separation and transfer efficiencies as the most significant factor are first taken into consideration, as they always dominantly affect the photocatalytic activity of semiconductor photocatalysts. Fig. 11a shows the transient photocurrent-time curves of 350 °C (BiOI), 410 °C (Bi<sub>4</sub>O<sub>5</sub>I<sub>2</sub>), 440 °C (Bi<sub>4</sub>O<sub>5</sub>I<sub>2</sub>-Bi<sub>5</sub>O<sub>7</sub>I) and 500 °C (Bi<sub>5</sub>O<sub>7</sub>I) samples, which can indicate the separation and movement dynamics of photoinduced charge carriers [40–42]. All the photoelectrodes manifest reversible and stable photocurrent response with light on and off. The Bi<sub>4</sub>O<sub>5</sub>I<sub>2</sub>-Bi<sub>5</sub>O<sub>7</sub>I composite exhibits the highest photocurrent intensity, and Bi<sub>4</sub>O<sub>5</sub>I<sub>2</sub> comes next, which is stronger than that of BiOI and Bi<sub>5</sub>O<sub>7</sub>I. The slightly higher photocurrent density of BiOI compared to Bi<sub>5</sub>O<sub>7</sub>I may be resulted from the intense light absorption of BiOI in visible light regions.

Electrochemical impedance spectra (EIS) were recorded to further affirm the interfacial charge transfer distinction that influences the photocatalytic activity [40–42]. As shown in Fig. 11b, it can be seen that Bi<sub>4</sub>O<sub>5</sub>I<sub>2</sub>-Bi<sub>5</sub>O<sub>7</sub>I reveals the smallest arc radius in the EIS Nyquist plots, and the enlarged order of arc radius is Bi<sub>4</sub>O<sub>5</sub>I<sub>2</sub> < Bi<sub>5</sub>O<sub>7</sub>I < BiOI. The smaller the arc radius is, the faster the interfacial charge migrates. Thus, the charge separation and transfer efficiency order is Bi<sub>4</sub>O<sub>5</sub>I<sub>2</sub>-Bi<sub>5</sub>O<sub>7</sub>I > Bi<sub>4</sub>O<sub>5</sub>I<sub>2</sub> > Bi<sub>5</sub>O<sub>7</sub>I > BiOI. The results from the current photoelectrochemical measurements are strictly in accordance with the above photodegradation tests, which disclose that the charge separation and transfer efficiency is primarily responsible for the photocatalytic activity of these bismuth iodides.

On the other hand, the band energy level also affects the photocatalytic activity of a single semiconductor and the band structure of semiconductor heterojunction. Herein, Mott-Schottky (M-S) method is employed to elucidate the band energy potentials and semiconductor types. The M-S plots of BiOI (350 °C sample), Bi<sub>4</sub>O<sub>5</sub>I<sub>2</sub> (410 °C sample) and Bi<sub>5</sub>O<sub>7</sub>I (500 °C sample) are illustrated in Fig. 12, the FB potentials are determined to be -0.07 V, -0.82 V and -0.61 V, respectively, versus a saturated calomel electrode (SCE). They are equal to 0.17 V, -0.58 V and -0.37 V vs. a normal hydrogen electrode (NHE). Due to the positive slope of 1/C<sup>2</sup> versus potential curve, BiOI, Bi<sub>4</sub>O<sub>5</sub>I<sub>2</sub> and Bi<sub>5</sub>O<sub>7</sub>I are herein n-type semiconductors with the CB position 0.1–0.3 eV higher than that of FB [43,44]. Thus, the CB positions of BiOI, Bi<sub>4</sub>O<sub>5</sub>I<sub>2</sub> and Bi<sub>5</sub>O<sub>7</sub>I are separately calculated as 0.07 V, -0.68 eV and -0.47 eV. Correspondingly, their VB levels are estimated to be 1.82 eV, 1.61 eV and 2.45 eV, respectively.

On the basis of the above results, the photocatalytic activity order of the samples 440 °C (Bi<sub>4</sub>O<sub>5</sub>I<sub>2</sub>-Bi<sub>5</sub>O<sub>7</sub>I) > 470 °C (Bi<sub>4</sub>O<sub>5</sub>I<sub>2</sub>-Bi<sub>5</sub>O<sub>7</sub>I) > 410 °C (Bi<sub>4</sub>O<sub>5</sub>I<sub>2</sub>) > 500 °C (Bi<sub>5</sub>O<sub>7</sub>I) > 350 °C (BiOI) can be explained as follows: For part I: the three pristine bismuth iodides (BiOI, Bi<sub>4</sub>O<sub>5</sub>I<sub>2</sub> and Bi<sub>5</sub>O<sub>7</sub>I), firstly, the charge separation and transfer efficiency order is Bi<sub>4</sub>O<sub>5</sub>I<sub>2</sub> > Bi<sub>5</sub>O<sub>7</sub>I > BiOI, which is strictly in agreement with their photocatalytic activity order. It demonstrates that charge separation efficiency is the crucial factor in determining the photocatalytic activity. Besides, the Bi<sub>4</sub>O<sub>5</sub>I<sub>2</sub> possesses the largest surface area compared to BiOI and Bi<sub>5</sub>O<sub>7</sub>I, which results in enhanced adsorption ability and more reaction active sites, favoring photochemical reaction. Though Bi<sub>5</sub>O<sub>7</sub>I has smaller surface area

than BiOI, the rational band structure with more negative CB potential and more positive VB level can enable the photogenerated  $\bullet\text{O}_2^-$  and  $\text{h}^+$  of  $\text{Bi}_5\text{O}_7\text{I}$  strong oxidation capability (Fig. 13a) [45]. Combined the charge separation and band structure advantages,  $\text{Bi}_5\text{O}_7\text{I}$  thus shows a better photocatalytic performance than BiOI. For part II: the composite bismuth iodides ( $\text{Bi}_4\text{O}_5\text{I}_2\text{-Bi}_5\text{O}_7\text{I}$ ), which displays the highest photocatalytic activity and outperforms  $\text{BiOI}$ ,  $\text{Bi}_4\text{O}_5\text{I}_2$  and  $\text{Bi}_5\text{O}_7\text{I}$ . According to the band structures of  $\text{Bi}_4\text{O}_5\text{I}_2$  and  $\text{Bi}_5\text{O}_7\text{I}$ , both the CB (-0.68 eV) and VB (1.61 eV) positions of  $\text{Bi}_4\text{O}_5\text{I}_2$  are more negative than that of  $\text{Bi}_5\text{O}_7\text{I}$  (CB -0.47 eV, VB 2.45 eV). Namely, the band structures of  $\text{Bi}_4\text{O}_5\text{I}_2$  and  $\text{Bi}_5\text{O}_7\text{I}$  are overlapped and staggered. Therefore,  $\text{Bi}_4\text{O}_5\text{I}_2$  and  $\text{Bi}_5\text{O}_7\text{I}$  can form an energy-structure matchable heterojunction, as depicted in Fig. 13b. In this heterojunction, the photo-excited electrons ( $e^-$ ) can be transferred from the CB of  $\text{Bi}_4\text{O}_5\text{I}_2$  to the CB of  $\text{Bi}_5\text{O}_7\text{I}$  by the offset of 0.21 eV, and meanwhile photogenerated holes ( $\text{h}^+$ ) easily migrate from the VB of  $\text{Bi}_5\text{O}_7\text{I}$  to the VB of  $\text{Bi}_4\text{O}_5\text{I}_2$  by the offset of 0.84 eV. Thus, the photogenerated  $e^-$  and  $\text{h}^+$  are separated effectively in  $\text{Bi}_4\text{O}_5\text{I}_2\text{-Bi}_5\text{O}_7\text{I}$  heterojunction, attributing to its higher photocatalytic activity than the pristine  $\text{Bi}_4\text{O}_5\text{I}_2$  and  $\text{Bi}_5\text{O}_7\text{I}$ .

#### 4. Conclusion

A series of bismuth oxyiodides, including  $\text{Bi}_4\text{O}_5\text{I}_2$ ,  $\text{Bi}_5\text{O}_7\text{I}$  and  $\text{Bi}_4\text{O}_5\text{I}_2\text{-Bi}_5\text{O}_7\text{I}$  phase-junction were obtained by facilely *in situ* calcinating  $\text{BiOI}$  microspheres. All these bismuth oxyiodides show 3D hierarchical architectures, which are assembled by different nano-building-units. The photoabsorption of samples was found to be orderly adjustable from 700 nm ( $\text{BiOI}$ ) to 400 nm ( $\text{Bi}_5\text{O}_7\text{I}$ ), which results in the tenability in oxidation and reduction ability of photocatalyst. Photodegradation for tetracycline hydrochloride, BPA and RhB demonstrated that  $\text{Bi}_4\text{O}_5\text{I}_2$  holds the best photocatalytic activity in the pure-phase bismuth oxyiodides for its relatively high charge separation efficiency and large surface area, and  $\text{Bi}_4\text{O}_5\text{I}_2\text{-Bi}_5\text{O}_7\text{I}$  displays the most prominent photocatalytic performance among all the samples owing to the efficient charge separation and transfer originated from band alignment of the as-formed phase-junction. It also displays high photochemical stability. Besides, the photocatalytic mechanism and degradation pathway are also surveyed. This work may further our understanding on controllable synthesis of agnate semiconductor photocatalysts with tunable photoactivity.

#### Competing interest

The authors declare no competing financial interest.

#### Acknowledgement

This work was jointly supported by the National Natural Science Foundations of China (Grant No. 51672258, 51302251 and 51572246), the Fundamental Research Funds for the Central Universities (2652015296).

#### Appendix A. Supplementary data

Supplementary data associated with this article can be found, in the online version, at <http://dx.doi.org/10.1016/j.apcatb.2016.10.082>.

#### References

- [1] M.A. Christopher, K.W. Parlett, A.F. Lee, Chem. Soc. Rev. 42 (2013) 3876–3893.
- [2] L. Zhang, H.B. Wu, S. Madhavi, H.H. Hng, X.W. Lou, J. Am. Chem. Soc. 134 (2012) 17388–17391.
- [3] H.K. Wang, A.L. Rogach, Chem. Mater. 26 (2014) 123–133.
- [4] A. Kubacka, M. Fernández-García, G. Coloín, Chem. Rev. 112 (2012) 1555–1614.
- [5] L. Shang, T. Bian, B. Zhang, D.H. Zhang, L.Z. Wu, C.H. Tung, Y.D. Yin, T.R. Zhang, Angew. Chem. Int. Ed. 53 (2014) 250–254.
- [6] H.L. Wang, L.S. Zhang, Z.G. Chen, J.Q. Hu, S.J. Li, Z.H. Wang, J.S. Liu, X.C. Wang, Chem. Soc. Rev. 43 (2014) 5234–5244.
- [7] X. Li, J.G. Yu, M. Jaroniec, Chem. Soc. Rev. 45 (2016) 2603–2636.
- [8] R. Edla, N. Patel, M. Orlandi, N. Bazzanella, V. Bello, C. Maurizio, G. Mattei, P. Mazzoldi, A. Miotello, Appl. Catal. B: Environ. 166–167 (2015) 475–484.
- [9] H.W. Huang, K. Xiao, Y. He, T.R. Zhang, F. Dong, X. Du, Y.H. Zhang, Appl. Catal. B: Environ. 199 (2016) 75–86.
- [10] H.W. Huang, Y. He, X. Du, P.K. Chu, Y.H. Zhang, ACS Sustainable Chem. Eng. 3 (2015) 3262–3273.
- [11] J. Li, L.J. Cai, J. Shang, Y. Yu, L.Z. Zhang, Adv. Mater. (2016), <http://dx.doi.org/10.1002/adma.201600301>.
- [12] Y.G. Zhou, Y.F. Zhang, M.S. Lin, J.L. Long, Z.Z. Zhang, H.X. Lin, J.C.-S. Wu, X.X. Wang, Nat. Commun. 6 (2016) 8340.
- [13] H.W. Huang, X.W. Li, J.J. Wang, F. Dong, P.K. Chu, T.R. Zhang, Y.H. Zhang, ACS Catal. 5 (2015) 4094–4103.
- [14] L. Chen, R. Huang, M. Xiong, Q. Yuan, J. He, J. Jia, M.Y. Yao, S.L. Luo, C.T. Au, S.F. Yin, Inorg. Chem. 52 (2013) 11118–11125.
- [15] L. Chen, J. He, Q. Yuan, Y. Liu, C.T. Au, S.F. Yin, J. Mater. Chem. A 3 (2015) 1096–1102.
- [16] L. Chen, R. Huang, S.F. Yin, S.L. Luo, C.T. Au, Chem. Eng. J. 193–194 (2012) 123–130.
- [17] L. Chen, S.F. Yin, S.L. Luo, R. Huang, Q. Zhang, T. Hong, C.T. Au, Ind. Eng. Chem. Res. 51 (2012) 6760–6768.
- [18] Q. Yuan, L. Chen, M. Xiong, J. He, S.L. Luo, C.T. Au, S.F. Yin, Chem. Eng. J. 255 (2014) 394–402.
- [19] H.F. Cheng, B.B. Huang, Y. Dai, Nanoscale 6 (2014) 2009–2026.
- [20] J. Li, Y. Yu, L.Z. Zhang, Nanoscale 6 (2014) 8473–8488.
- [21] H. Li, J. Shang, Z.H. Ai, L.Z. Zhang, J. Am. Chem. Soc. 137 (2015) 6393–6399.
- [22] Y.H. Wu, B. Yuan, M.R. Li, W.H. Zhang, Y. Liu, C. Li, Chem. Sci. 6 (2015) 1873–1878.
- [23] L.M. Sun, L. Xiang, X. Zhao, C.J. Jia, J. Yang, Z. Jin, X.F. Cheng, W.L. Fan, ACS Catal. 5 (2015) 3540–3551.
- [24] X. Xiao, C. Liu, R.P. Hu, X.X. Zuo, J.M. Nan, L.S. Li, L.S. Wang, J. Mater. Chem. 22 (2012) 22840–22843.
- [25] Q.C. Liu, D.K. Ma, Y.Y. Hu, Y.W. Zeng, S.M. Huang, ACS Appl. Mater. Interfaces 5 (2013) 11927–11934.
- [26] H.W. Huang, X. Han, X.W. Li, S.C. Wang, P.K. Chu, Y.H. Zhang, ACS Appl. Mater. Interfaces 7 (2015) 482–492.
- [27] F. Dong, T. Xiong, Y.J. Sun, Y.X. Zhang, Y. Zhou, Chem. Commun. 51 (2015) 8249–8252.
- [28] Y.F. Liu, W.Q. Yao, D. Liu, R.L. Zong, M. Zhang, X.G. Ma, Y.F. Zhu, Appl. Catal. B: Environ. 163 (2015) 547–553.
- [29] X. Zhang, L.Z. Zhang, T.F. Xie, D.J. Wang, J. Phys. Chem. C 113 (2009) 7371–7378.
- [30] Y.Y. Li, H.C. Yao, J.S. Wang, N. Wang, Z.J. Li, Mater. Res. Bull. 46 (2011) 292–296.
- [31] M.C. Long, P.D. Hu, H.D. Wu, Y.Y. Chen, B.H. Tan, W.M. Cai, J. Mater. Chem. A 3 (2015) 5592–5598.
- [32] X. Xiao, R. Hao, X.X. Zuo, J.M. Nan, L.S. Li, W.D. Zhang, Chem. Eng. J. 209 (2012) 293–300.
- [33] X. Xiao, C. Xing, G. He, X. Zuo, J. Nan, L. Wang, Appl. Catal. B: Environ. 148–149 (2014) 154–163.
- [34] S. Sun, W. Wang, L. Zhang, L. Zhou, W. Yin, M. Shang, Environ. Sci. Technol. 43 (2009) 2005–2010.
- [35] J. Cao, X. Li, H.L. Lin, B.Y. Xu, B.D. Luo, S.F. Chen, Mater. Lett. 76 (2012) 181–183.
- [36] Y. Bai, L.Q. Ye, L. Wang, X. Shi, P.Q. Wang, W. Bai, P.K. Wong, Appl. Catal. B: Environ. 194 (2016) 98–104.
- [37] Y. Bai, T. Chen, P.Q. Wang, L. Wang, L.Q. Ye, Chem. Eng. J. 304 (2016) 454–460.
- [38] Y. Ohko, K. Hashimoto, A. Fujishima, J. Phys. Chem. A. 101 (1997) 8057–8062.
- [39] S.W. Gao, C.S. Guo, J.P. Lv, Q. Wang, Y. Zhang, S. Hou, J.F. Gao, J. Xu, Chem. Eng. J. (2017), <http://dx.doi.org/10.1016/j.cej.2016.09.032>.
- [40] X.J. Bai, L. Wang, Y.F. Zhu, ACS Catal. 2 (2012) 2769–2778.
- [41] H.W. Huang, Y. He, Z.S. Lin, L. Kang, Y.H. Zhang, J. Phys. Chem. C 117 (2013) 22986–22994.
- [42] H.W. Huang, K. Liu, K. Chen, Y.L. Zhang, Y.H. Zhang, S.C. Wang, J. Phys. Chem. C 118 (2014) 14379–14387.
- [43] N. Tian, H.W. Huang, C.Y. Liu, F. Dong, T.R. Zhang, X. Du, S.X. Yu, Y.H. Zhang, J. Mater. Chem. A 3 (2015) 17120–17129.
- [44] H.W. Huang, Y. He, X.W. Li, M. Li, C. Zeng, F. Dong, X. Du, T.R. Zhang, Y.H. Zhang, J. Mater. Chem. A 3 (2015) 24547–24556.
- [45] J.G. Yu, J.X. Low, W. Xiao, P. Zhou, M. Jaroniec, J. Am. Chem. Soc. 136 (2014) 8839–8842.